A NOVEL DEFORMABLE LIMIT ANALYSIS MODELING FOR THE MASONRY ARCH OR VAULT STRUCTURES

YIWEI HUA[*] AND GABRIELE MILANI[*]

[*] Department of Architecture, Built Environment and Construction Engineering
Politecnico di Milano
Piazza Leonardo da Vinci 32, 20133 Milan, Italy
e-mail: yiwei.hua@polimi.it, gabriele.milani@polimi.it.

Key words: Limit analysis, Masonry arch, Kinematic theorem, Collapse mechanism, Load-bearing capacity.

Summary. Regarding the limit analysis modeling of the masonry system, the employment of rigid elements seems to be a generally acknowledged solution. It could be correct for some cases where the block involves a simple stress state, for instance, vertically compressed wall, while it may not be a reasonable modeling for the masonry arch or vault masonry since the combination of bending and compression should lead to a more complicated stress distribution. Consideration of the deformability of the block element could be necessary in this case. In this paper, we develop a novel brick element for the limit analysis modeling of the ring or vault structures. This element takes into account the deformation induced by both bending and axial compressing motions. A new limit analysis formulation is established according to the kinematic theorem. We first construct the element velocity field referring to the classical beam theory, and the new compatibility condition for the deformable brick elements can then be obtained. A linear constitutive based on the No-tensile-resistance (NTR) assumption is employed to describe the material behavior of the brick. After collecting all the updated conditions, we give the new limit analysis formulation for the proposed deformable brick element. Implementing the proposed theory, we perform two collapse analyses as bench-mark studies to understand the influence of rigid or deformable modeling for the ring. The results indicate the employment of rigid or deformable modeling for the ring can lead to very distinct collapse performance. In the investigation of the 80-block arch, the presence of the deformed bricks leads to a moderate overall motion of the arch. The capacity prediction is also more conservative against the rigid modeling case. Regarding the case of the Prestwood bridge, a more flexible ring modeling will reduce the passive deformation of the backfill upon the ring. As a result, both dissipation and potential power in the backfill decrease, and the predicted collapse load is much lower. Finally, the load prediction in the Prestwood bridge case is comparable to the on-site experimental outcomes carried out in the last century. The accuracy of the proposed element is thus demonstrated.

1 INTRODUCTION

Masonry arch or vault structures comprise a large proportion of architectural heritage in both Western and Eastern worlds, due to their aesthetic construction and reliable structural performance. However, those buildings are still vulnerable in some extreme circumstances because of the cracks and damage that exist. Therefore, to provide an effective improvement on their structure behavior as well as necessary preventive conservation, comprehensive numerical simulation in a priori is required to understand their capacity and collapse behavior under different scenarios. Thanks to the development of Computational Operations Research in recent decades, limit analysis has become a standard and rapid approach to investigating the collapse of masonry systems, which can conveniently take into account the discontinuities at the interface and the real brick arrangement of the masonry.

In the current contributions of limit analysis, rigid block modeling for masonry bricks seems to be a widely acknowledged solution, which has been proven reasonable when applied to masonry walls or aggregates [1-5]. Nevertheless, Gilbert et al. [6] once reported that using rigid elements to model the ring of the masonry arch bridge may give rise to an overestimated capacity prediction, in particular when the backfill upon the ring is included. On the contrary, the employment of deformable-beam modeling, proposed by Cavicchi and Gambarotta [7-8], produced an accurate collapse load, being very comparable to the on-site test. This has indicated that the consideration of brick deformability may be necessary in some scenarios.

Despite the excellent performance of the beam element modeling proposed by Cavicchi and Gambarotta [7-8], such reliability could not be expected in more general circumstances due to the neglect of the real thickness of the arch. This paper extends the conceptualization of this element to construct a deformable 4-node brick element. We develop the formulation for this new element based on the Upper Bound (UB) theory. The geometric compatibility condition and constitutive model for the new brick element are first developed and the new limit analysis optimization with consideration of the element deformability is then proposed. As an implementation, we present two collapse analyses as case studies: one 80-block arch and one arch bridge that involves ring-fill interaction. In each case, the results from rigid and deformable arch modeling are compared, through which the effect of the ring deformability in different cases can be shed light.

2 METHODOLOGIES

Below we will briefly demonstrate the construction of the governing equations of the upper bound (UB) limit analysis for the novel brick elements.

$$\mathbf{u}^i\left(\mathbf{r}^i\right) = \mathbf{u}_{\mathcal{R}}^i\left(\mathbf{r}^i\right) + \mathbf{u}_{\mathcal{A}}^i\left(\mathbf{r}^i\right) = \mathbf{H}_{\mathcal{R}}^i\left(\mathbf{r}^i\right)\mathbf{u}_{\mathcal{R}}^i + \mathbf{H}_{\mathcal{A}}^i\left(\mathbf{r}^i\right)\mathbf{u}_{\mathcal{A}}^i$$

$$\mathbf{H}_{\mathcal{R}}^i\left(\mathbf{r}^i\right) = \begin{bmatrix} 1 & 0 & -\left(y-\overline{y}^i\right) \\ 0 & 1 & \left(x-\overline{x}^i\right) \end{bmatrix}, \ \mathbf{H}_{\mathcal{A}}^i\left(\mathbf{r}^i\right) = \mathbf{e}_{\alpha}^i\left[\mathbf{r}^i\cdot\mathbf{e}_{\alpha} \quad \left(\mathbf{r}^i\cdot\mathbf{e}_{\alpha}^i\right)\left(\mathbf{r}^i\cdot\mathbf{e}_{\beta}^i\right)\right] \tag{1}$$

$$\mathbf{u}_{\mathcal{R}}^i := \begin{bmatrix} u^i & v^i & \omega^i \end{bmatrix}^T, \ \mathbf{u}_{\mathcal{A}}^i := \begin{bmatrix} \varepsilon_{\alpha}^i & \kappa^i \end{bmatrix}^T$$

The kinematic mode of this element can be regarded as a superposition of rigid body motion $\mathbf{u}_{\mathcal{R}}\left(\mathbf{r}\right)$ and axial deformation mode $\mathbf{u}_{\mathcal{A}}\left(\mathbf{r}\right)$ induced by the axial force and bending moment (Eq.

(1)). Here, the construction of the axial deformation space refers to the classical beam theory (see Figure 1a). Introducing the axial strain ε_α and curvature κ, the velocity field induced by this deformation mode can be described. In this element, only deformation along the axial direction $\mathbf{e}_\alpha$ is allowed and the strain distribution along the height of the section is linear.

$$\mathbf{q}_j = \begin{bmatrix} -\left(\mathbf{A}^a_{j,\mathcal{R}}\right)^T & \left(\mathbf{A}^b_{j,\mathcal{R}}\right)^T \end{bmatrix} \begin{bmatrix} \mathbf{u}^a_\mathcal{R} \\ \mathbf{u}^b_\mathcal{R} \end{bmatrix} + \begin{bmatrix} -\left(\mathbf{A}^a_{j,\mathcal{A}}\right)^T & \left(\mathbf{A}^b_{j,\mathcal{A}}\right)^T \end{bmatrix} \begin{bmatrix} \mathbf{u}^a_\mathcal{A} \\ \mathbf{u}^b_\mathcal{A} \end{bmatrix}$$

$$\mathbf{A}^i_{j,\mathcal{R}} = \begin{bmatrix} \mathbf{Q}_j \mathbf{H}^i_\mathcal{R}\left(\mathbf{r}^i_1\right) \\ \mathbf{Q}_j \mathbf{H}^i_\mathcal{R}\left(\mathbf{r}^i_2\right) \end{bmatrix}^T , \quad \mathbf{A}^i_{j,\mathcal{A}} = \begin{bmatrix} \mathbf{Q}_j \mathbf{H}^i_\mathcal{A}\left(\mathbf{r}^i_1\right) \\ \mathbf{Q}_j \mathbf{H}^i_\mathcal{A}\left(\mathbf{r}^i_2\right) \end{bmatrix}^T , \quad i = a, b \tag{2}$$

$$\mathbf{Q}_j = \begin{bmatrix} \mathbf{e}^j_n & \mathbf{e}^j_t \end{bmatrix}^T$$

$$\mathbf{A}^T_\mathcal{R} \mathbf{u}_\mathcal{R} + \mathbf{A}^T_\mathcal{A} \mathbf{u}_\mathcal{A} = \mathbf{q} \tag{3}$$

After defining the element kinematic mode, we can proceed to compute the interfacial discontinuities across the elements. We subtract the velocity at the overlapped nodes of blocks a and b (Figure 1b) and then use the rotational matrix $\mathbf{Q}_j$ to project this subtraction from the global frame $(\mathbf{e}_x, \mathbf{e}_y)$ to the interfacial one $(\mathbf{e}_n, \mathbf{e}_t)$ (Eq. (2)). Assembling the equation at the element level, the global compatibility condition can be stated as a linear equality (Eq. (3)).
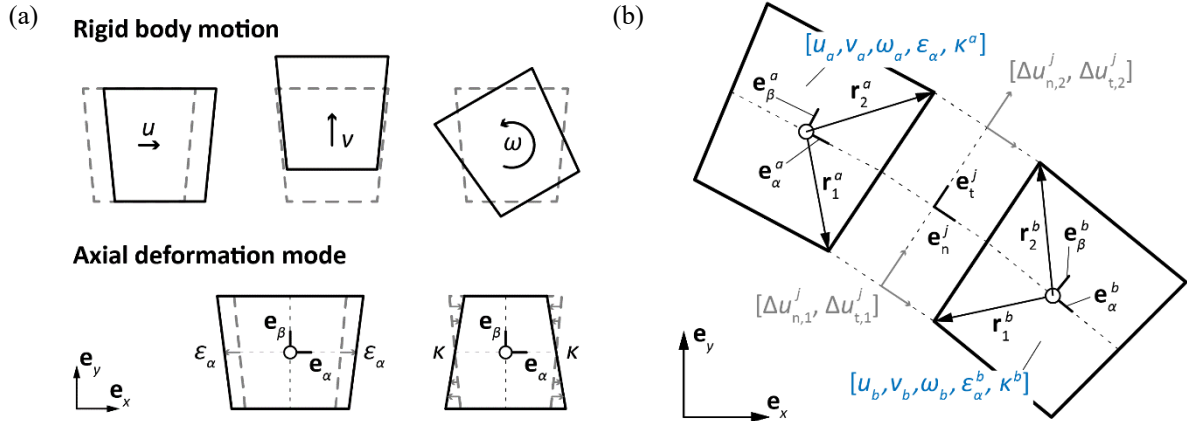

Figure 1: Configuration of the novel deformable block element: (a) element kinematic mode; (b) computation of interfacial velocity jumps, geometric compatibility.

$$F_b\left(\tilde{N}, \tilde{M}\right) = \begin{cases} \dfrac{\tilde{N}}{Ab} + \dfrac{\left|\tilde{M}\right|}{Wb} - \sigma_t \le 0 \\[3mm] -\dfrac{\tilde{N}}{Ab} + \dfrac{\left|\tilde{M}\right|}{Wb} - \sigma_c \le 0 \end{cases}, \quad W = \dfrac{hd^2}{4}, \ A = hd, \ \tilde{N} := Nb, \ \tilde{M} := Mb \tag{4}$$

Recall that the strain field along the sectional height is known, which can be decomposed to a uniform distribution and a centrosymmetric-linear distribution. We can further deduce the

sectional stress distribution based on the assumption of rigid plasticity (**Figure 2**a). Therefore, a straightforward conceptualization of the constitutive model for the new brick element is to require the maximum tensile and compressive stress of the section to be in the span of the corresponding limit, i.e. Eq. (4). Here, b, h and d represent the width, height and depth of the block, respectively; W and A denote the plastic modulus and the area of the section.

$$\mathbf{M}\tilde{\boldsymbol{\sigma}} - \mathbf{z}_1 = \mathbf{c}_1, \quad \tilde{\boldsymbol{\sigma}}_i := \begin{bmatrix} \tilde{N}_i & \tilde{M}_i \end{bmatrix}^T, \quad \mathbf{z}_i := \begin{bmatrix} z_i^{1+} & z_i^{1-} & z_i^{2+} & z_i^{2-} \end{bmatrix}^T \leq 0 \tag{5}$$

$$\mathbf{M}_i = \begin{bmatrix} \dfrac{1}{A_i b_i} & -\dfrac{1}{A_i b_i} & \dfrac{1}{A_i b_i} & -\dfrac{1}{A_i b_i} \\[2mm] -\dfrac{1}{W_i b_i} & \dfrac{1}{W_i b_i} & \dfrac{1}{W_i b_i} & -\dfrac{1}{W_i b_i} \end{bmatrix}^T, \quad \mathbf{c}_i := \begin{bmatrix} \sigma_t & \sigma_c & \sigma_t & \sigma_c \end{bmatrix}^T \tag{6}$$

We can also rewrite Eq. (4) as a linear equality Eq. (5) by introducing the non-positive slackness variables $\mathbf{z}_1$. For specific element i, expressions of the constitutive operator $\mathbf{M}$ and cohesion vector $\mathbf{c}_1$ are given in Eq. (6). Figure 2b manifests that the region of the static-allowed force state defined by this constitutive law is a quadrilateral zone. The flow rule for the proposed element is associated with the yield surface. Thus, we can directly construct the corresponding flow constraint Eq. (7) through the mapping operator $\mathbf{M}^T$, which is the transpose of the constitutive operator.

$$\mathbf{M}^T \boldsymbol{\lambda} = \mathbf{u}_\mathcal{A}, \quad \boldsymbol{\lambda}_i := \begin{bmatrix} \lambda_i^{1+} & \lambda_i^{1-} & \lambda_i^{2+} & \lambda_i^{2-} \end{bmatrix}^T \geq 0 \tag{7}$$
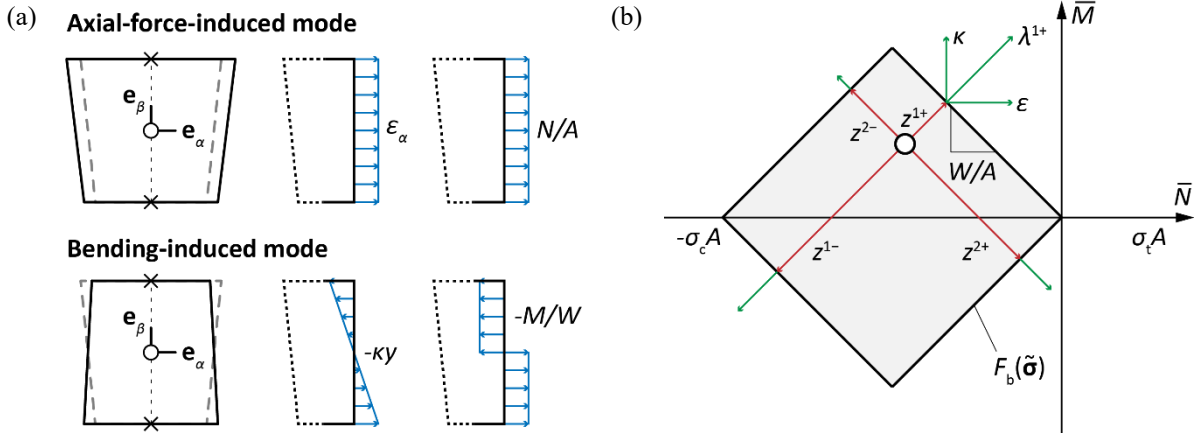

Figure 2: (a) assumption of strain and stress distribution for element; (b) diagram of the limit domain for the proposed constitutive model.

Finally, we compute the dissipation energy of the element due to the deformation (Eq. (8)). Integrating strain energy density over the bulk and applying the constitutive and flow relations (Eqs. (5) and (7)), it can eventually be expressed by the inner product of cohesion $\mathbf{c}_1$ and plastic multiplier vector $\boldsymbol{\lambda}$.

Collecting all the new governing equations accounting for the element deformation, we can

now establish the optimization formulation for limit analysis based on Upper Bound (UB) theory. In the constraint list of the new optimization problem (Eq. (9)), we update the geometric compatibility condition (3) and supplement an extra flow rule for the deformation unknowns (7). The first constraint is the positive external work condition [9] and the third one represents the flow rule for the interfaces, which is associated with the well-acknowledged Mohr-Coulomb friction model (see [10-11] for more details). In the objective function, the dissipation induced by the element deformation has also been taken into account. If we dismiss all the terms in Eq. (9) that account for the deformability of the element, the optimization will return to the standard rigid block limit analysis (Eq. (11)) (see [11-12]).

$$
\begin{aligned}
\dot{W}_{\mathrm{D}}^{e} &= \sum_{i=1}^{N_{\mathrm{E}}} \int_{V} \sigma^{i}\left(y_{\beta}\right) \varepsilon^{i}\left(y_{\beta}\right) dV \\
&= d \sum_{i=1}^{N_{\mathrm{E}}} b_{i}\left(\int_{0}^{h_{i}/2}\left(\frac{\tilde{N}_{i}}{A_{i}b_{i}} - \frac{\tilde{M}_{i}}{W_{i}b_{i}} \right)\left(\varepsilon_{\alpha}^{i} - \kappa^{i}y_{\beta}\right) + \int_{-h_{i}/2}^{0}\left(\frac{\tilde{N}_{i}}{A_{i}b_{i}} + \frac{\tilde{M}_{i}}{W_{i}b_{i}} \right)\left(\varepsilon_{\alpha}^{i} - \kappa^{i}y_{\beta}\right) \right) dy_{\beta} \\
&= \sum_{i=1}^{N_{\mathrm{E}}} \tilde{N}_{i}\varepsilon_{\alpha}^{i} + \tilde{M}_{i}\kappa^{i} = \tilde{\boldsymbol{\sigma}}^{T}\boldsymbol{\varepsilon} = \tilde{\boldsymbol{\sigma}}^{T}\mathbf{M}^{T}\boldsymbol{\lambda} = \mathbf{c}_{1}^{T}\boldsymbol{\lambda}
\end{aligned} \tag{8}
$$

Table 1: Formulations for rigid or deformable limit analysis

	UPPER BOUND LIMIT ANALYSIS	LOWER BOUND LIMIT ANALYSIS
DEFORMABLE CASE	minimize $\quad -\mathbf{f}_{D}^{T}\mathbf{u}_{\mathcal{R}} + \mathbf{c}_{0}^{T}\mathbf{p} + \mathbf{c}_{1}^{T}\boldsymbol{\lambda}$ subject to $\quad \mathbf{f}_{L}^{T}\mathbf{u}_{\mathcal{R}} = 1$ $\qquad \mathbf{A}_{\mathcal{R}}^{T}\mathbf{u}_{\mathcal{R}} + \mathbf{A}_{\mathcal{A}}^{T}\mathbf{u}_{\mathcal{A}} = \mathbf{q}$ (9) $\qquad \mathbf{N}^{T}\mathbf{p} = \mathbf{q}, \mathbf{p} \geq 0$ $\qquad \mathbf{M}^{T}\boldsymbol{\lambda} = \mathbf{u}_{\mathcal{A}}, \boldsymbol{\lambda} \geq 0$	maximize $\quad \alpha$ subject to $\quad \mathbf{A}_{\mathcal{R}}\mathbf{x} = \alpha\mathbf{f}_{L} + \mathbf{f}_{D}$ $\qquad \mathbf{A}_{\mathcal{A}}\mathbf{x} + \tilde{\boldsymbol{\sigma}} = 0$ (10) $\qquad \mathbf{N}\mathbf{x} - \mathbf{z}_{0} = \mathbf{c}_{0}, \mathbf{z}_{0} \leq 0$ $\qquad \mathbf{M}\tilde{\boldsymbol{\sigma}} - \mathbf{z}_{1} = \mathbf{c}_{1}, \mathbf{z}_{1} \leq 0$
RIGID CASE	minimize $\quad -\mathbf{f}_{D}^{T}\mathbf{u}_{\mathcal{R}} + \mathbf{c}_{0}^{T}\mathbf{p}$ subject to $\quad \mathbf{f}_{L}^{T}\mathbf{u}_{\mathcal{R}} = 1$ $\qquad \mathbf{A}_{\mathcal{R}}^{T}\mathbf{u}_{\mathcal{R}} = \mathbf{q}$ (11) $\qquad \mathbf{N}^{T}\mathbf{p} = \mathbf{q}, \ \mathbf{p} \geq 0$	maximize $\quad \alpha$ subject to $\quad \mathbf{A}_{\mathcal{R}}\mathbf{x} = \alpha\mathbf{f}_{L} + \mathbf{f}_{D}$ (12) $\qquad \mathbf{N}\mathbf{x} - \mathbf{z}_{0} = \mathbf{c}_{0}, \mathbf{z}_{0} \leq 0$

Observing the duality of Upper Bound (UB) formulation (Eq. (9)), we can get the Lower Bound (LB) optimization problem (Eq. (10)). Compared with the corresponding formulation for the rigid element (Eq. (12)), extra balance condition and constitutive constraint need to be supplemented for the in-element generalized force $\tilde{\boldsymbol{\sigma}}$ late introduced.

3   RESULTS

Implementing the proposed formulation, in this section we will present two case studies to investigate the performance of the proposed element. In each case, the collapse results from the

new deformable bricks will be compared to the prediction from rigid block modeling, through which we can shed light on the influence of different considerations of the ring flexibility when analyzing the masonry arch structures.

3.1 Case Study A: an 80-block arch ring

The first benchmark study is to investigate the collapse of a circular arch ring with 80 blocks. The geometry feature of the arch is illustrated in Figure 3, with an out-of-plane depth of 3800 mm. We consider a concentrated load applied at (approximately) a quarter of the arch. The material properties of the element follow the set of [7-8], listed in Table 2. Note that here the tensile strength of the brick is equal to zero. The brick is regarded as standard No-tensile-resistance (NTR) material in this case. The collapse of the deformable ring and rigid ring is solved by Eqs. (9) and (11), respectively.
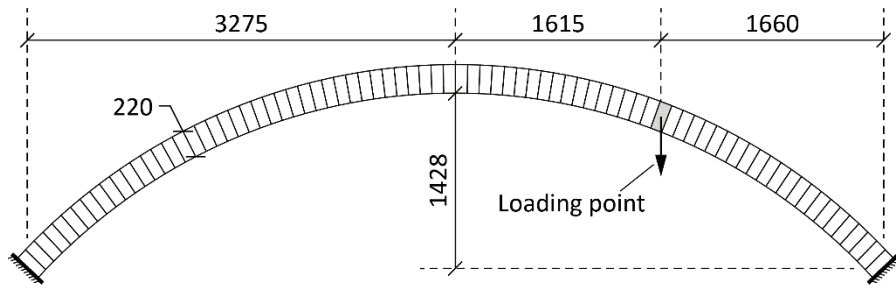

Figure 3: Geometry and load/boundary conditions of the 80-block ring.

Table 2: Material feature of the bricks in the case of the 80-block ring

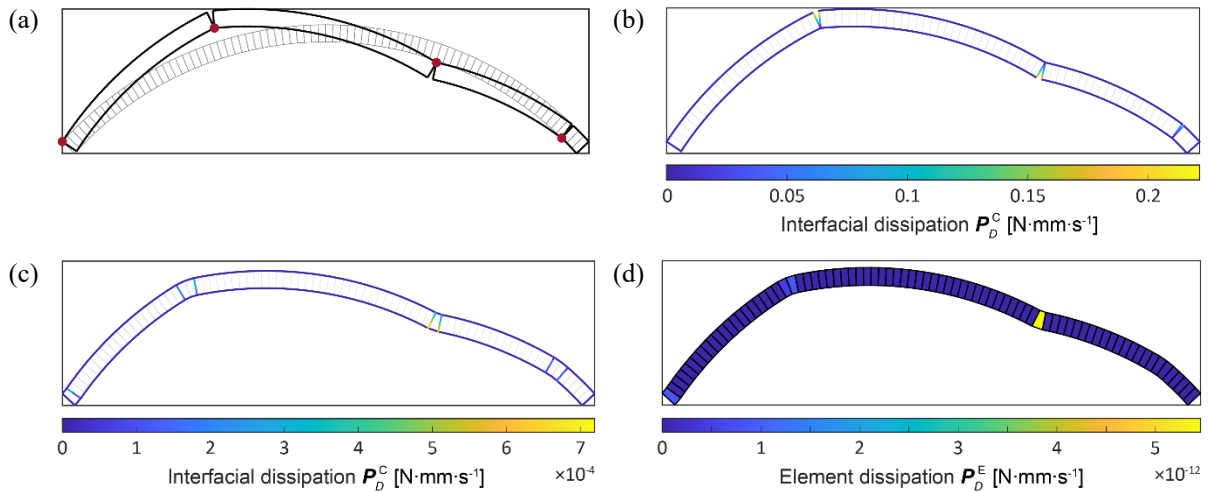| Density ρ_b [kg/m³]	Interfacial cohesion c_{bb} [MPa]	Compressive strength σ_{bc} [MPa]	Tensile strength σ_{bt} [MPa]	Frictional angle φ_{bb} [°]
2000	10^{-6}	4.5	0	37

Figure 4: Collapse of 80-block ring: (a) rigid case, mechanism; (b) rigid case, interfacial dissipation, $P_u = 41.414$ kN; (c) deformable case, interfacial dissipation; (b) deformable case, in-element dissipation, $P_u = 17.598$ kN.

6

In the rigid modeling case, the arch collapses as a standard 4-hinge (S4H) mechanism (Figure 4a), which is widely observed in other contributions (see [10-11]). Extrados hinges are located near the loading brick and left springer stone while intrados hinges appear at the left quarter and right springer. After considering the brick deformability, the collapse mechanism of the ring changes. The rotational separations at the interfaces, originally taking place in the rigid case, now vanish, being instead by the deformation of the brick, and the position of these bending bricks is consistent with the hinge location of the standard 4-hinge collapse (compare Figure 4b and Figure 4c). Remark that the dissipation of these deformed bricks is almost zero, indicating that such failure is caused by the high bending moment rather than crushing. As a result, the overall motion of the ring is significantly moderated; the potential power of the system decreases. Given the infinitesimal system dissipation in this case, the drop in the potential power of the mechanism will directly impact the capacity prediction of the structure. Finally, the collapse capacity of the deformable ring is 57.5% lower than the rigid one.

3.2 Case Study B: Prestwood Bridge

We now move to investigate the collapse of another more practical benchmark case: Prestwood Bridge, a real single-span masonry arch bridge being numerically and experimentally investigated by previous researchers. In this case, we explicitly consider the fill upon the arch to understand how the ring deformability affects the collapse involving arch-ring interaction. The geometry characteristic of the model is given in Figure 5. The out-of-plane depth of the bridge is also 3800 mm. The load condition is a surface pressure (with a width of 300 mm) against the fill applied at the quarter-span of the bridge. The boundary conditions of the model are all unilateral contacts (Figure 5).
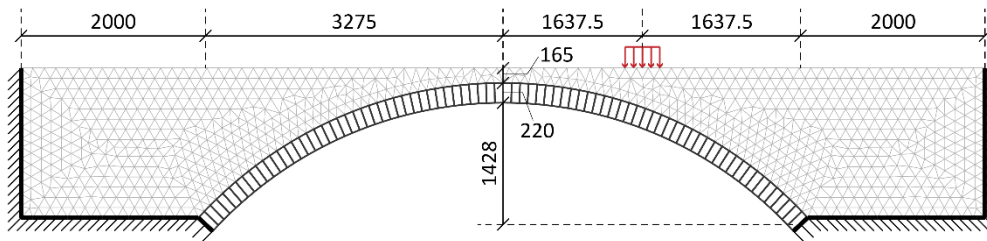

Figure 5: Geometric characteristics, backfill mesh, and load/boundary conditions of Prestwood Bridge.

The backfill behavior is modeled by constant-strain triangular elements developed by Sloan and Kleeman in 1995 [17], applying Mohr-Coulomb constitutive with tension cut-off [6-7,14]. To avoid the non-linearity in the constraint, the linearization technique is employed to approximate the real yield surface into several planes [15]. As the compatibility condition, constitutive, and flow rule share the same matrix expression as those in the previous deduction, Eq. (9) can continue to be used in this case study despite the combined usage of these triangular and brick elements. We generate the triangular mesh of the backfill region through a MATLAB-based generator "MESH2D" [16], with a typical size of 131 mm (see mesh in Figure 5). Material parameters for the brick, backfill, and interfaces all follow the setting of the numerical work from previous researchers [7-8], which have been calibrated in their works based on the exper-

imental results (Table 3). Again, we will compare the collapse performance of the bridge employing the rigid or deformable ring modeling.

Table 3: Material parameters for the brick, backfill and interfaces in the case of Prestwood Bridge.

	Elements	
	Density ρ_b [kg/m^3]	2000
brick	Compressive strength σ_{bc} [MPa]	4.5
	Tensile strength σ_{bt} [MPa]	0
	Density ρ_f [kg/m^3]	2000
backfill	Frictional angle φ_f [°]	37
	Cohesion c_f [MPa]	0.01
	Tensile strength σ_{ft} [MPa]	0
	Interfaces	
Frictional angle	Brick to brick φ_{bb} [°]	37
	Brick to backfill φ_{bf} [°]	37
	Backfill to backfill φ_{ff} [°]	37
	Brick to brick c_{bb} [MPa]	10^{-6}
Cohesion	Brick to backfill c_{bf} [MPa]	10^{-6}
	Backfill to backfill c_{ff} [MPa]	0.01

Figure 6 illustrates the collapse of the bridge employing the rigid ring modeling. The deformation of the ring part is analogous to the 4-hinge mechanism observed in the pure-arch case, yet with the occurrence of multiple hinges in one location. For instance, we can note a group of intrados hinges appears near the keystone and right springer. The magnitude of the relative rotation reduces though, which could be attributed to the containment effect of the backfill. In terms of the backfill motion, a trapezoid region at the right settles downward due to the external vertical pressure, and the backfill at the left inverted-triangular region is extruded up, caused by the passive movement of the ring. The element dissipation and crack propagation majorly take place in these two regions of the backfill as well. Finally, we notice a load dispersion in the backfill part: the distance between the two extrados hinges below the pressure is much boarder than the original width of the load.

The capacity of the system is significantly cut down after using the deformable brick to model the arch ring (with a drop of 46.3% against the prediction of the rigid case) and this prediction is exceptionally consistent with the experimental study [17] (with only a bias of 0.98%). In this case, the ring part presents a more flexible behavior when the bridge collapses (see Figure 7). The interfacial discontinuities vanish, being shared by the zero-dissipation bricks whose failure again results from the large bending moment. The weakened deformation of the arch ring further gives rise to a lower dissipation in the backfill. Compared with the prediction of the rigid case, the location of the left bending bricks gets closer to the keystone, and the extruding effect of the ring against the backfill is relieved. Therefore, we observe a shrunk passive-extruded area at the left of the backfill. Given also the moderated overall motion of the backfill part, the dissipation and potential power of the system both decrease when the ring deformability improves. This explains the considerable decrease in the load prediction after
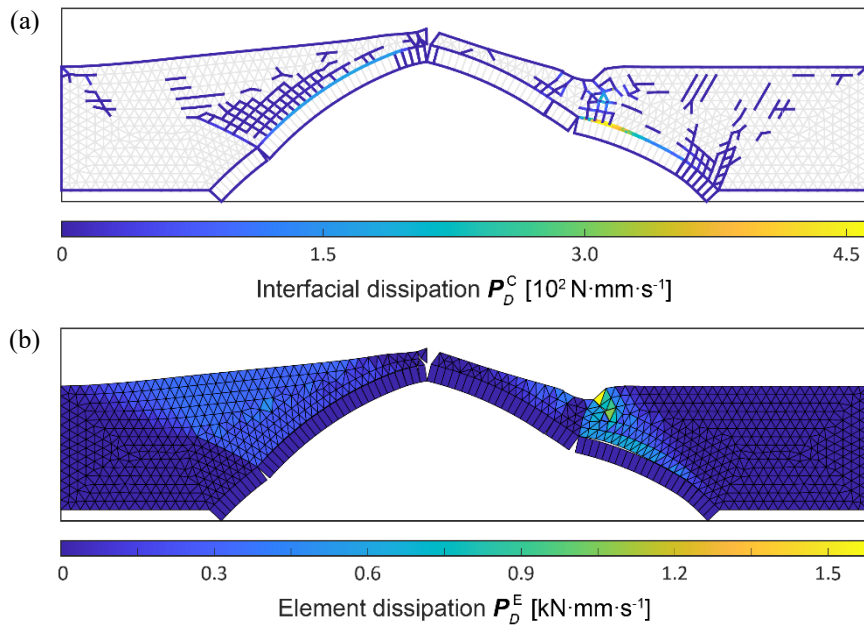
using a more deformable ring modeling.

Figure 6: Collapse of Prestwood Bridge, rigid arch ring, $P_\mathrm{u} = 420.462$ kN: (a) interfacial dissipation; (b) in-element dissipation.
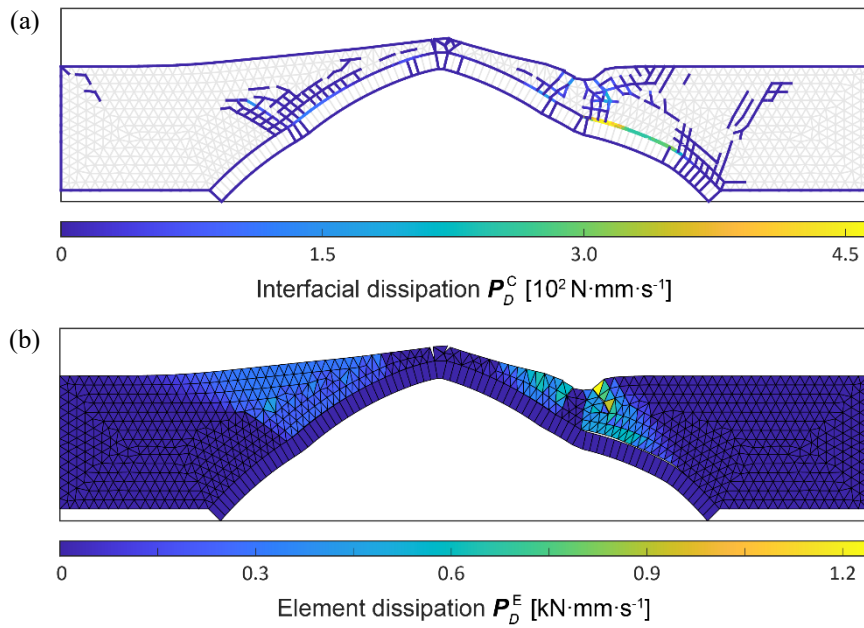

Figure 7. Collapse of Prestwood Bridge, deformable arch ring, $P_\mathrm{u} = 225.747$ kN: (a) interfacial dissipation; (b) in-element dissipation.

9

4   CONCLUSIONS

This paper has proposed a novel deformable brick element for limit analysis, which could be an alternative when modeling the deformability of masonry arch or vault structures. The kinematic mode of the new element includes both the rigid body motion and the axial deformation that mimics the bending-compression behavior of the beam elements. A flow rule associated with a No-tension resistance (NTR) yield criterion has been employed to constrain the plastic flow of the brick. The new limit analysis formalization can be stated as a standard Linear Programming (LP) problem. For the sake of benchmarking, two collapse analyses have been conducted to test the robustness of the proposed element, and we have summarized the influence mechanism of the ring deformability in these two different cases.

In the case of the 80-block arch, the deformability of the arch brick majorly influences the potential power of the system. The presence of the deformed bulks will remarkably reduce the kinematic magnitude of the ring, and its collapse capacity thus drops (57.5%) compared with that of the rigid ring. In the collapse of Prestwood bridge, the ring deformability manifests a more noticeable impact on the behavior of the backfill, particularly the passive-extrusion zone. A weaker extrusion from the ring will give rise to a more moderate deformation of the backfill region, leading to a reduction of passive-extruded backfill. As a result, the predicted load also decreases against that of the rigid modeling because of the reduction of the dissipation and potential power of the backfill. Moreover, the reliability of our proposed deformable bricks is also verified by comparison with the previous experimental results [17] (deviation within 0.98%). In conclusion, this element can be a proper approach to modeling the deformability of masonry arch or vault structures.

REFERENCES

[1]   Portioli FPA, 2020. "Rigid block modelling of historic masonry structures using mathematical programming: a unified formulation for non-linear time history, static pushover and limit equilibrium analysis." Bull Earthq Eng 18:211–239. https://doi.org/10.1007/s10518-019-00722-0

[2]   Gilbert M, Casapulla C, Ahmed HM, 2006. "Limit analysis of masonry block structures with non-associative frictional joints using linear programming." Comput Struct 84:873–887. https://doi.org/10.1016/j.compstruc.2006.02.005

[3]   Wang P, Milani G, 2023. "Seismic vulnerability prediction of masonry aggregates: Iterative Finite element Upper Bound limit analysis approximating no tensile resistance." Eng Struct 293:116595. https://doi.org/10.1016/j.engstruct.2023.116595

[4]   Grillanda N, Valente M, Milani G, 2020. "ANUB-Aggregates: a fully automatic NURBS-based software for advanced local failure analyses of historical masonry aggregates." Bull Earthq Eng 18:3935–3961. https://doi.org/10.1007/s10518-020-00848-6

[5]   Grillanda N, Valente M, Milani G, et al, 2020. "Advanced numerical strategies for seismic assessment of historical masonry aggregates." Eng Struct 212:110441. https://doi.org/10.1016/j.engstruct.2020.110441

[6] Gilbert M, Nguyen D, Smith C, 2007. "Computational limit analysis of soil-arch inter-action in masonry arch bridges." In *Proc 5th Int Conf arch Bridg ARCH* 633–640

[7] Cavicchi A, Gambarotta L, 2005. "Collapse analysis of masonry bridges taking into account arch-fill interaction." Eng Struct 27:605–615. https://doi.org/10.1016/j.eng-struct.2004.12.002

[8] Cavicchi A, Gambarotta L, 2006. "Two-dimensional finite element upper bound limit analysis of masonry bridges." Comput Struct 84:2316–2328. https://doi.org/10.1016/j.compstruc.2006.08.048

[9] Maier G, Nappi A, 1990. "A theory of no-tension discretized structural systems." Eng Struct 12:227–234. https://doi.org/10.1016/0141-0296(90)90021-J

[10] Hua Y, Milani G, 2023. "Simple modeling of reinforced masonry arches for associated and non-associated heterogeneous limit analysis." Comput Struct 280:. https://doi.org/10.1016/j.compstruc.2023.106987

[11] Hua Y, Milani G, 2022. "Rigid Block Limit Analysis of Masonry Arches with Associated and Non-associated Slides." In: *From Corbel Arches to Double Curvature Vaults: Analysis, Conservation and Restoration of Architectural Heritage Masonry Structures*. pp 169–203

[12] Ferris MC, Tin-Loi F, 2001. "Limit analysis of frictional block assemblies as a mathematical program with complementarity constraints." Int J Mech Sci 43:209–224. https://doi.org/10.1016/S0020-7403(99)00111-3

[13] Sloan SW, Kleeman PW, 1995. "Upper bound limit analysis using discontinuous velocity fields." Comput Methods Appl Mech Eng 127:293–314. https://doi.org/10.1016/0045-7825(95)00868-1

[14] Drucker DC, 1954. "Coulomb Friction, Plasticity, and Limit Loads." J Appl Mech 21:71–74. https://doi.org/10.1115/1.4010821

[15] Bottero A, Negre R, Pastor J, Turgeman S, 1980. "Finite element method and limit analysis theory for soil mechanics problems." Comput Methods Appl Mech Eng 22:131–149. https://doi.org/10.1016/0045-7825(80)90055-9

[16] Engwirda D, 2014. "Locally-optimal Delaunay-refinement and optimisation-based mesh generation." The University of Sydney

[17] Page J, 1995. "Load Tests to Collapse on Masonry Arch Bridges." Arch Bridg 289–298. https://doi.org/10.1680/ab.20481.0029